SCIENCE CHINA
Information Sciences

April 2021, Vol. 64 140402:1–140402:14
https://doi.org/10.1007/s11432-020-3172-1

• REVIEW •

Special Focus on Two-Dimensional Materials and Device Applications

Properties and photodetector applications of two-dimensional black arsenic phosphorus and black phosphorus

Ruyue HAN[1,2†], Shun FENG[1,3†], Dong-Ming SUN[1,2*] & Hui-Ming CHENG[1,2,4*]

[1]*Shenyang National Laboratory for Materials Science, Institute of Metal Research, Chinese Academy of Sciences, Shenyang* 110016*, China;*
[2]*School of Materials Science and Engineering, University of Science and Technology of China, Shenyang* 110016*, China;*
[3]*School of Physical Science and Technology, ShanghaiTech University, Shanghai* 200031*, China;*
[4]*Shenzhen Geim Graphene Center, Shenzhen International Graduate School, Tsinghua University, Shenzhen* 518055*, China*

Received 14 December 2020/Revised 11 January 2021/Accepted 13 January 2021/Published online 8 March 2021

Abstract Two-dimensional (2D) black arsenic phosphorus (b-AsP), as an alloy of black phosphorus (b-P) with arsenic, has attracted great attention because of its outstanding electronic and optical properties, including high carrier mobility, tunable bandgap and in-plane anisotropy. B-AsP has a smaller bandgap (0.15–0.3 eV) than the b-P bandgap (0.3–2.0 eV), and thus can be used for mid-infrared photodetectors. In addition, both of them can form various van der Waals (vdW) heterojunctions with other 2D materials to realize novel functional optoelectronic devices. Here, we compare the basic characteristics of b-AsP and b-P, including crystal structure, optical properties, band structure, electrical properties and stability, and we summarize the update progress of b-AsP in photo detection, including representatives of phototransistor and photodiode devices. In the last part, the future research directions are discussed.

Keywords black arsenic phosphorus, crystal structure, optical property, electrical property, photodetector

Citation Han R Y, Feng S, Sun D-M, et al. Properties and photodetector applications of two-dimensional black arsenic phosphorus and black phosphorus. Sci China Inf Sci, 2021, 64(4): 140402, https://doi.org/10.1007/s11432-020-3172-1

1 Introduction

Black phosphorus (b-P) was synthesized by phase transition of white phosphorus under high pressure in 1914 [1], and it was reported that the bulk b-P was a kind of semiconductor in 1986, but its quality was too difficult to control and it hardly attracted people's interest [2]. Mechanical exfoliation and transfer technology has developed rapidly since graphene was discovered [3–6], and two-dimensional (2D) b-P has received widespread attention [7]. In 2014, several groups revealed the properties of monolayer or few-layer b-P through theoretical calculations and experiments, which shows outstanding properties, such as tunable bandgap [8], in-plane anisotropy [9] and high carrier mobility [10].

Interestingly, by introducing arsenic into b-P using a high pressure process, a new material named black arsenic phosphorus (b-AsP) can be synthesized [11], and this bulk material exhibits superconducting characteristics at a low temperature of about 10 K. In 2015, layered b-AsP was first reported as an infrared semiconductor with tunable composition and bandgap (0.15–0.3 eV) [12], so it is suitable for near- and middle-infrared photo detection. At the same time, layered b-AsP can form various van der Waals (vdW) heterojunctions with other 2D materials, thereby providing a method for fabricating a new type of high-performance photodetectors [13–16].

Compared with the widely studied b-P, there are fewer studies on b-AsP. In this forward-looking review, we adopt a strategy to compare b-P and b-AsP from the basic properties to applications in the photo detection field, aiming to provide some promising directions for the future research on b-AsP. We

---

[*] Corresponding author (email: dmsun@imr.ac.cn, cheng@imr.ac.cn)
[†] Han R Y and Feng S have the same contribution to this work.

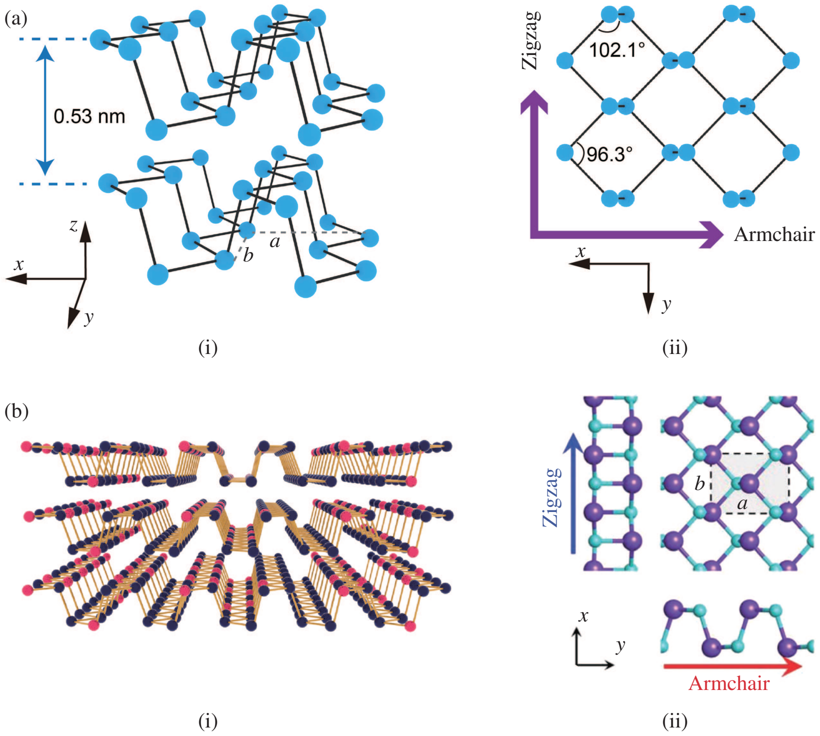

Figure 1 (Color online) Crystal structures of b-P and b-AsP. (a-i) Perspective view of b-P crystal structure. The spacing of interlayer is 0.53 nm. (a-ii) Top view of monolayer b-P, where x and y correspond to the directions of armchair and zigzag, respectively. (b-i) Perspective view of b-AsP crystal lattice. (b-ii) Crystal lattice of the monolayer b-AsP in top and side views. (b-ii) is reproduced with permission from [21].

first introduce the basic properties of b-P and b-AsP, including crystal structure, optical properties, band structure, electrical properties and stability. Subsequently, we summarize the update of b-P and b-AsP for photo detection, such as phototransistors and photodiodes. Finally, the future research directions are discussed.

2 Properties

2.1 Crystal structure

To understand the crystal of b-AsP, the structure of b-P should be considered. In a monolayer b-P, there are two atomic layers including two kinds of P-P bonds, which are divided into the short bond and the long bond by length. As for the short bond in the crystal, which is connected by the two nearest phosphorus atoms in the same atomic layer with a bond length of 0.2224 nm. While the long bond consists of two nearest phosphorus atoms from top and bottom atomic layer, showing a bond length of 0.2244 nm (Figure 1(a-i)). As shown in Figure 1(a-ii), from the top view, the lattice of b-P shows an irregular hexagonal structure with two kinds of bond angles. The larger bond angle is consisted of two short bonds, showing a value of 102.1°, and the smaller angle is consisted of a short bond and a long bond, showing a value of 96.3° [17, 18]. In addition, the puckered structure of monolayer b-P reduces the symmetry of the parent isotropic structure, and only one two-fold rotation and one mirror plane are contained in the lattice structure [19, 20] (Figure 1(a-ii)).

The atomic structure of b-AsP is similar to that of b-P, shown in Figure 1(b-i). This crystal also has a puckered structure with irregular hexagonal structure. From the top view, the two nearest phosphorus or arsenic atoms along the armchair direction show a crystal constant of 4.60 Å, while the two nearest phosphorus or arsenic atoms along the zigzag direction show a crystal constant of 3.51 Å (Figure 1(b-ii)) [21]. In addition to theoretical calculations, experimental data are more credible. The crystal structure of b-AsP can be obtained by characterizing the high resolution transmission electron microscope (TEM). From the high resolution TEM image of the b-AsP flake, the orthorhombic crystal structure is shown and the crystal constant along different directions can be measured. The crystal constant along armchair

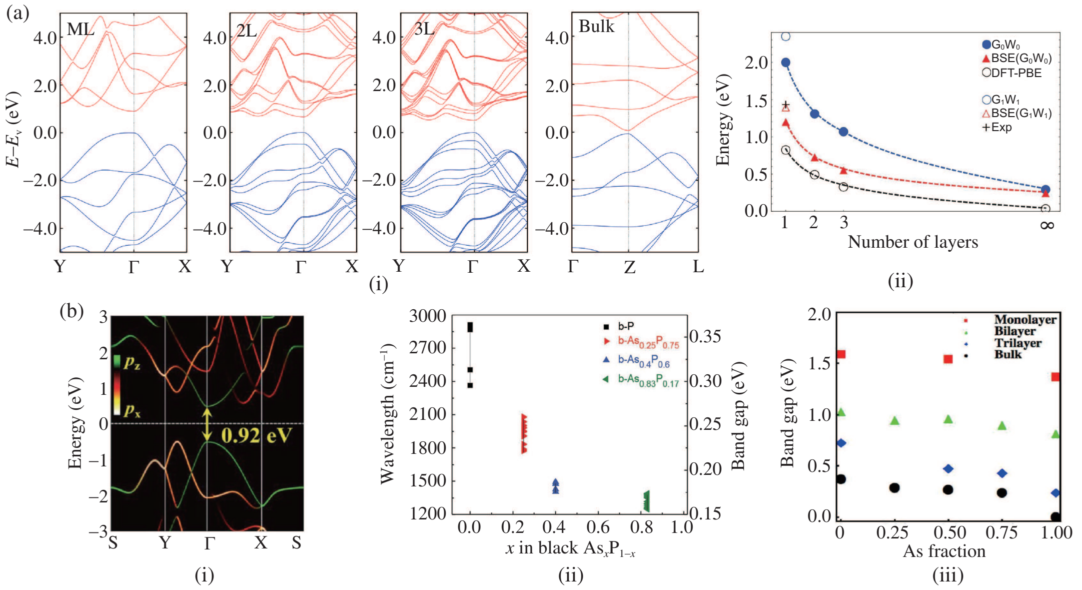

Figure 2 (Color online) Band structures of b-P and b-AsP. (a-i) Band structures of one-layer, two-layers, three-layers and bulk phosphorene calculated using density functional theory. (a-ii) The relationship between bandgap and the layer number in theory and experiment. (b-i) b-AsP's orbital-resolved band structure obtained from first principles calculations coupled with the function formalism of non-equilibrium green. (b-ii) Component of arsenic dependent bandgaps of thick b-As$_x$P$_{1-x}$ flakes (> 30 nm). (b-iii) Bandgaps of b-As$_x$P$_{1-x}$ determined by the arsenic component and number of layers, calculated by HSE06 method. (a-i) is reproduced with permission from [30], (a-ii) from [8], (b-i) from [21], (b-ii) from [12], and (b-iii) from [31].

direction is 3.3 Å and along zigzag direction is 4.7 Å [22], which is agree with the calculation results [21]. The crystal constant of b-P along armchair direction is about 4.4 Å, which is smaller than that of b-AsP, indicating that the increase of arsenic atoms leads to an increase of the lattice constant. Therefore, b-AsP has the similar crystal structure as b-P, but a larger lattice constant than b-P [22]. The puckered honeycomb configuration of b-AsP results in its highly anisotropy electronic [23], thermal [24–26] and optical properties [12, 27–29].

2.2 Band structure

Figure 2 [8, 12, 21, 30, 31] shows the band structures of b-P and b-AsP. Monolayer and bulk b-P show all direct bandgaps [8, 32]. With the increase number of layers, the bandgap of b-P reveals a redshift which decreases from 2.0 eV (monolayer) to 0.3 eV (bulk) (Figure 2(a-i)) [30]. The bandgap as a function of the thickness is calculated by the GW method, as shown in Figure 2(a-ii). Experimental and theoretical bandgaps of all materials exhibit some differences, which are ascribed to different conditions [8, 33].

For the band structure of monolayer b-AsP, several theoretical calculations show a direct bandgap at around 0.92 eV [21, 23, 34]. Sun et al. [23] calculated the bandgap of monolayer b-AsP using first principles calculations method, which ranges from 0.92 to 0.95 eV owing to the increase of the component of phosphorus. Zhou et al. [21] reported similar results from first principles calculations coupled with the function formalism of non-equilibrium green (Figure 2(b-i)). In thick b-As$_x$P$_{1-x}$ materials (>30 nm), the bandgap is decreased with increasing arsenic content (Figure 2(b-ii)) [12]. The bandgap of b-As$_x$P$_{1-x}$ is decreased sharply when the arsenic content increases from $x = 0$ to 0.25 and decreases more slowly when the arsenic content increases further to $x = 0.4$ and finally to $x = 0.83$. At the same time, the bandgaps of b-AsP with the same composition are also different. Each date point in Figure 2(b-ii) corresponds to the measurement result from the same b-AsP flakes using different polarization angles or from b-AsP flakes with the same composition but different thicknesses, resulting in different of bandgap values. Wu et al. [14] reported a clear p-type band structure of multi-layer b-AsP (10.8 nm) with a bandgap of 0.25 eV and a work function of 4.4 eV. However, some groups calculated smaller or larger b-AsP bandgaps than 0.92 eV [26, 28]. The relationship between material thickness and bandgaps is shown in Figure 2(b). As the thickness increases, the bandgaps of these two materials will decrease obviously (Figure 2(b-iii)). In general, the bandgap monolayer, few-layer, and bulk b-AsP are smaller than that of b-P [31].

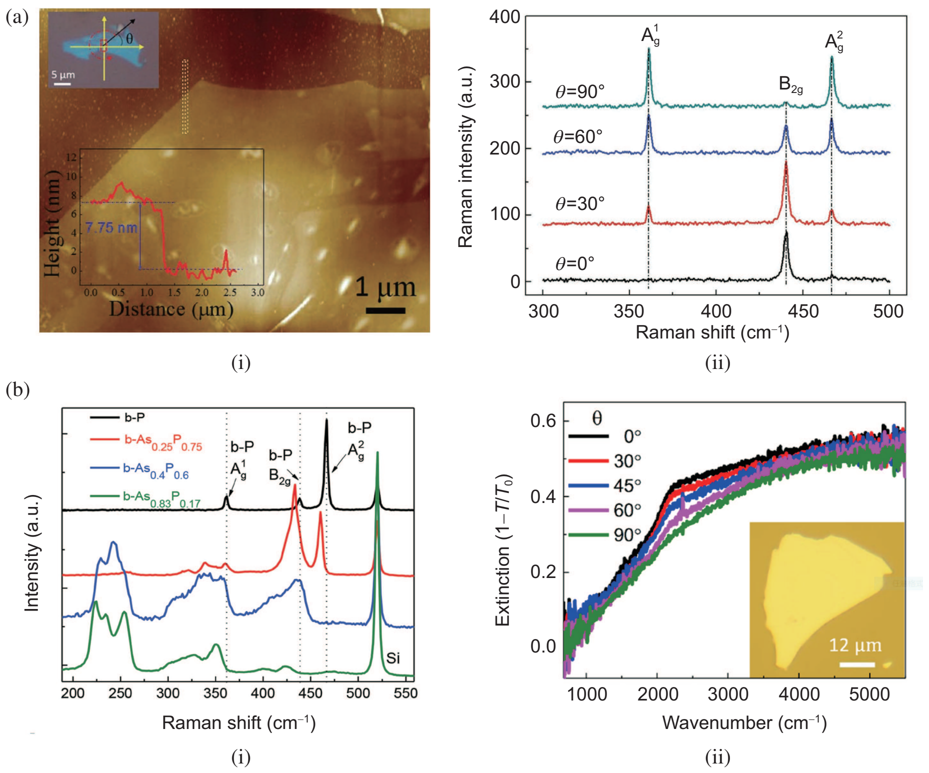

Figure 3 (Color online) Optical properties of b-P and b-AsP. (a-i) An atomic force microscopy image of a thin b-P flake, shows a thickness about 7.75 nm. Inset: optical image of this b-P flake. (a-ii) Raman spectrum of b-P using polarized laser excitation along different directions. (b-i) Raman spectra of b-AsP with different contents of arsenic. (b-ii) Polarized infrared extinction spectra of the b-$As_{0.83}P_{0.17}$. Inset: optical image of the characterized flake. (a-i) and (a-ii) are reproduced with permission from [35], (b-i) from [12], and (b-ii) from [29].

2.3 Optical properties

Three peaks at 365, 440, and 470 cm^{-1} correspond to the A_g^1, B_{2g}, and A_g^2 vibration modes of b-P, respectively [35–41]. As shown in Figure 3(a-i), an atomic force microscopy image of a thin b-P flake shows a thickness of 7.75 nm [35]. An optical image of this b-P is shown in the inset of Figure 3(a-i). The Raman spectra of this flake obtained at different polarizations is shown in Figure 3(a-ii). The intensity of the A_{2g} mode decreases obviously with increasing polarization of the excitation laser from $0°(x)$ to $90°(y)$, because the main atomic vibration of the A_{2g} mode is in the x direction (armchair). So that the crystal orientation of monolayer b-P can be identified by polarization-resolved Raman spectroscopy [35]. When the b-P flake is illuminated by a polarized incident infrared light from the z direction, and the incident light is polarized along six directions, which ranges from 0° to 330° with a step of 30°, all polarized directions of the infrared spectra show obvious increase at 2400 cm^{-1}, corresponding to a bandgap of 0.3 eV [19].

Three major regimes are divided in the Raman spectra of b-AsP according to frequency. The low-frequency, medium-frequency and high-frequency regimes correspond to 200–300 cm^{-1}, 300–380 cm^{-1} and 380–500 cm^{-1}, respectively. For b-$As_{0.83}P_{0.17}$, three peaks at 256, 233, and 224 $\mathrm{cm}^{-1}$are detected in the low-frequency regime, which are assigned to the A_g^2, B_{2g} and A_g^1 modes, respectively (Figure 3(b-i)) [12,28]. As the increase of phosphorus content, a gradual redshift of peaks is discovered. In comparison with b-P, b-AsP exhibits more Raman peaks, which is agreement with the existence of heteroatomic P-As bond (Figure 3(b-i)) [12]. As shown in Figure 3(b-ii) inset, a 188 nm-thick b-$As_{0.83}P_{0.17}$ flake is fabricated using a mechanical exfoliation method. The polarization-resolved extinction spectra of this flake is measured using an infrared light, and shows an obvious increase at around 1000 cm^{-1}, corresponding to the bandgap of 0.124 eV [29]. The family of b-As_xP_{1-x} with different arsenic content ($x = 0$, 0.25, 0.4, and 0.83) is studied using polarization-resolved infrared absorption systematically [12]. As the increase of x in b-As_xP_{1-x}, the absorption edges of b-AsP shift to shorter wavelengths clearly, indicating that the bandgap of b-As_xP_{1-x} is decreased with increasing the amount of arsenic.

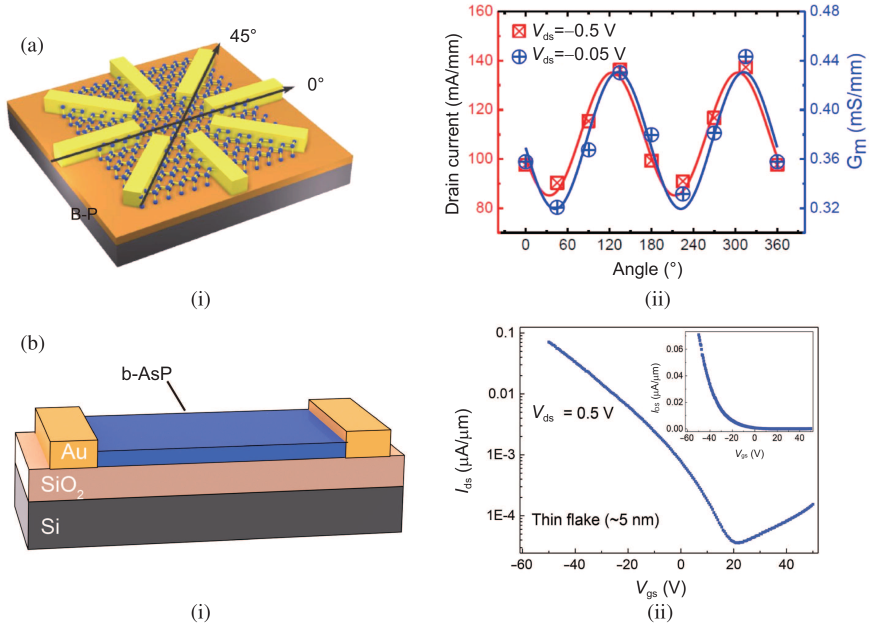

Figure 4 (Color online) Electronic properties of b-P and b-AsP. (a-i) Schematic of b-P device structure with eight electrodes along with different directions. (a-ii) The $I_{\rm ds}$ and the transconductance as a function of angle. (b-i) Schematic of a b-AsP based field-effect transistor. (b-ii) Transfer curve of a thin b-$\rm As_{0.83}P_{0.17}$ flake in semilog scale and linear scale (inset). (a-i) and (a-ii) are reproduced with permission from [9], (b-ii) from [12].

2.4 Electronic properties

In 2014, Liu et al. [9] first reported a field effect transistor based on few-layer b-P. In this device, a hole mobility of 286 $\rm cm^2{\cdot}V^{-1}{\cdot}\ s^{-1}$and an on/off ratio of 10^4 are achieved. The electrical transport of this device along different directions is different, showing an anisotropic property (Figures 4(a-i) and (a-ii)). Almost at the same time, a 10 nm-thick b-P field-effect transistor was fabricated by Li et al. [10], showing an high hole mobility about 1000 $\rm cm^2{\cdot}V^{-1}{\cdot}\ s^{-1}$ and a high on/off ratio in the order of 10^5. These studies initiated the research on b-P based nanoelectronic applications [33, 40–58]. To further improve the performance of b-P based field-effect transistors, devices with different thicknesses, contact electrodes, dielectric properties, and passivation layers have been fabricated (see details in Table 1 [9, 10, 12, 13, 19, 29, 42, 44, 46, 50, 52, 53, 56, 58–74]). Table 1 shows that transistors with ultrahigh hole mobility are mainly based on Cr/Au contact [10, 66], and the mobility is further improved by hBN passivation [68, 70]. For b-P based field-effect transistors, intrinsic ambipolar transfer characteristics have been widely observed owing to electrostatic modulation under an external electrical field, while the ambipolar behavior of b-P is always asymmetrical because of much lower electron concentration and mobility. The most direct way to improve the electron mobility of b-P is by n-type doping with $\rm Cs_2CO_3$, Al, Cu, and other dopants [52–58, 65, 66, 68, 70, 72, 73]. By contact-metal engineering, n-type field-effect transistors can also be realized. For example, black phosphorus with Al contact and a flake thickness of 13 nm exhibits unipolar to ambipolar transition with an electron mobility of up to 950 $\rm cm^2{\cdot}V^{-1}{\cdot}\ s^{-1}$ [71].

Field-effect transistors based on b-AsP typically have on/off ratios lower than 10^4 owing to their small bandgaps. As shown in Figure 4(b-i), a field-effect transistor is fabricated using a thin b-$\rm As_{0.83}P_{0.17}$ flake. The transfer curve of this device is shown in Figure 4(b-ii) [12]. The device has an ambipolar transport behavior with an on/off ratio about 1.9×10^3. By increasing the thickness from 11 to 21 nm, the on/off current ratio of b-AsP is decreased rapidly from 10^3 to 1.2 [16]. Although theoretical calculation shows that the mobility of b-AsP is higher than 10000 $\rm cm^2{\cdot}V^{-1}{\cdot}s^{-1}$ [69], the experimental mobility is in the range of 80–310 $\rm cm^2{\cdot}V^{-1}{\cdot}s^{-1}$ [13, 29]. As shown in Table 1, the mobility of b-AsP is much lower than that of b-P. Therefore, improvement in electrical performance of b-AsP is highly needed.

2.5 Material stability

For the production of new devices from emerging materials, the long-term stability of devices needs to be first demonstrated [75–77]. However, 2D b-P is unstable in air and reacts with oxygen. The researchers

Table 1 Electrical performance of b-AsP and b-P based field-effect transistors[a)]

Materials	Thickness (nm)	Contact electrode	Dielectric layer	Passivation layer	Mobility ($cm^2 \cdot V^{-1} \cdot s^{-1}$)	Ref.
ex b-$As_{0.83}P_{0.17}$	5–20	Ti-Au	SiO_2	PMMA	$h = 307$	[13]
ex b-$As_{0.83}P_{0.17}$	37	Cr-Au	hBN-SiO_2	hBN	$h = 79$, $e = 83$	[29]
ex b-$As_{0.83}P_{0.17}$	15	Ti-Au	SiO_2	PMMA	$h = 110$	[12]
cal b-AsP	1-layer	–	–	–	$h = 2100$, $e = 14380$	[59]
ex b-P	5–25	Ti-Au	Al_2O_3	Al_2O_3	$h = 200$	[60]
ex b-P	8	Ti-Au	SiO_2	–	$h = 100$, $e = 0.5$	[61]
ex b-P	4.5	Ti-Au	SiO_2	PMMA	$h = 142$	[62]
ex b-P	6–7	Ti-Au	hBN	–	$h = 25$, $e = 0.12$	[63]
ex b-P	5–15	Ti-Au	SiO_2	–	$h = 52$	[44]
ex b-P	20	Ti-Au	SiO_2	Al_2O_3	$h = 0.96$	[64]
ex b-P	4.8	Ti-Au	SiO_2	–	$h = 215$, $e = 1$	[65]
				Cs_2CO_3	$e = 27$	
				MoO_3	$h = 200$	
ex Se doped b-P	–	Cr-Au	SiO_2	–	$h = 561$	[66]
ex b-P	–	Au	SiO_2	Al_2O_3	$h = 100$	[67]
ex b-P	11.3	Ti-Au	Al_2O_3	Al_2O_3	$h = 187$	[53]
ex b-P	7	Au	SiO_2	Al_2O_3	$h = 230$	[56]
ex b-P	10	Ti-Au	SiO_2	–	$h = 286$	[9]
ex b-P	6.5	Cr-Au	SiO_2	–	$h = 984$	[10]
ex b-P	5	Ti-Pd	SiO_2	–	$h = 205$	[19]
ex b-P	1.9	Ti	SiO_2	Al_2O_3	$h = 172$, $e = 38$	[42]
ex b-P	8	Cr-Au	hBN-SiO_2	hBN	$h = 1350$	[68]
ex b-P	–	Au	hBN-SiO_2	–	$h = 400$, $e = 83$	[46]
ex b-P	43±2	Ti-Au	SiO_2	MMA-PMMA	$h = 900$	[69]
ex b-P	–	Cr-Au	hBN-SiO_2	hBN	$h = 5200$	[70]
ex b-P	13	AL	SiO_2	Al_2O_3	$e = 950$	[71]
	3				$e = 275$	
ex Al doped b-P	5	Ti-Au	SiO_2	Al_2O_3	$e = 1495$	[72]
ex Cu doped b-P	10	Ti-Au	hBN	–	$e = 690$	[73]
ex b-P	18.7	Ni	SiO_2	–	$h = 170$	[74]
		Pd			$h = 186$	
ex b-P	15	Ti-Au	Al_2O_3	Al_2O_3	$h = 310$, $e = 89$	[50]
ex b-P	13	Ti-Au	Al_2O_3	PMMA	$h = 233$	[52]
cal b-P	1-layer	–	–	–	$h = 26000$, $e = 1140$	[58]
	multi-layer				$h = 6400$, $e = 1580$	

a) ex: experimental results; cal: calculated results; *h*: hole mobility, *e*: electron mobility; PMMA: polymethyl methacrylate; MMA: methyl methacrylate.

found that there is a chemisorption process between oxygen and the lone pairs of phosphorus atoms at the surface of b-P [78–81]. The chemisorption of oxygen leads to the formation of oxygen defects, which makes the surface of phosphorene hydrophilic and forms a mixture of oxide and phosphoric acid. At the same time, the oxidation of 2D b-P can be accelerated by photons, and the phosphorus oxide can further be transformed into aqueous phosphoric acid with the help of water vapor, resulting in the poor stability of naked b-P devices in air [82]. Although the detailed degradation process of b-AsP devices has not been reported, their behavior may be similar to that of b-P devices. Up to now, several surface passivation strategies for b-P and b-AsP have been reported and the stability of devices can be dramatically improved. It has been shown that b-P encapsulated by aluminum oxide (Al_2O_3) keeps long term stable in air [29, 50, 67, 83, 84]. Without encapsulation, bubbles develop quickly on the b-P surface [60]. Moreover, b-P and b-AsP sandwiched between hBN layers exhibits long term stability in ambient conditions and even under the irradiation of strong laser [45, 68, 85, 86]. In addition to covering b-P with hBN or oxide by atomic layer deposition, organic molecules also are a good choice to prevent degradation and keep long term device stability [13, 16, 55, 69, 87, 88]. There are many encapsulation methods that have demonstrated long term effectiveness and can be used to device development in the future. Moreover, different types of defects in b-P can affect the stability in theory [89, 90]. Therefore,

Table 2 Performance of b-AsP based photodetectors[a)]

Material	Th (nm)	Device structure	Wavelength (nm)	R (mA/W)	EQE (%)	Speed (ms)	D^* (cm^2 V^{-1} s^{-1})	Ref.
b-AsP	25–35	Phototransistor	4600	–	8	0.0124, 0.0089	2.4×10^{10}	[27]
b-AsP	188	Phototransistor	3400	190	–	–	–	[29]
			5000	16				
			7700	1.2				
b-AsP	5–20	Phototransistor	3662	180	6.1	0.54, 0.52	1.06×10^{8}	[13]
MoS_2-b-AsP	–	Photodiode	4290	115.4	3.33	–	4.9×10^{9}	[13]
			2360	216.1	11.36		9.2×10^{9}	
MoS_2-b-AsP	66, 59	Photodiode	520	0.3	71	0.009, 0.005	–	[16]
InSe-b-AsP	10, 11.5	Photodiode	520	1000	1.5	0.217, 0.089	1×10^{12}	[14]

a) Th: thickness. R: responsivity, $R = I_{\mathrm{ph}}/P_{\mathrm{in}}$, where I_{ph} is photocurrent and P_{in} is incident light power. EQE $= hcR\lambda^{-1}e^{-1}$, where h is the Planck constant, c is the speed of light, and e is the electron charge. D^*: detectivity, defined by $D^* = \frac{R\sqrt{AB}}{S_n}$, where A is the active area, B is the electrical bandwidth, and S_n is the noise spectral density. Response speed: rise time is defined as from 10% to 90% of the photocurrent and fall time is defined as from 90% to 10% of the photocurrent.

defects in b-P plays a key role in the degradation process, which indicates that the stability of b-P can be enhanced by improving the material quality.

3 Photodetector applications

Photodetectors are widely used in applications of imaging, optical guidance, optical communication, remote sensing, etc. Various 2D materials such as graphene [91, 92], transition metal dichalcogenides [93–95], b-P and b-AsP have been exploited for photodetectors. High responsivity, fast response speed and broadband of detection have been the main challenge for 2D materials based photodetectors. The disadvantage of graphene is that it has no natural bandgap with a low response to light, while transition metal dichalcogenides are limited by large bandgaps so that they are mainly used for visible light detection. In contrast, b-P possesses a tunable bandgap at about 0.3–2.0 eV, allowing for photo detection in a large spectral range from ultraviolet to infrared [20, 38, 43, 44, 56, 61, 62, 67, 84, 92–111]. Interestingly, the b-AsP's bandgap is about 0.15–0.3 eV, which is smaller than that of b-P and can be used for mid-infrared photodetectors [12, 13, 27].

For b-P based photodetectors, various studies on phototransistors, photodiodes, plasmonics [40, 64, 101], and waveguides [104, 109–111] have been reported. However, less studies are reported on b-AsP based photodetectors, which mainly focus on phototransistors and photodiodes. In this section, we will introduce phototransistor and photodiode applications of b-P and b-AsP. We compared the structure and performance of photodetectors of these two materials to find new research directions for b-AsP based photodetectors.

The performance of photodetectors is commonly characterized by several figures of merit, such as external quantum efficiency (EQE), responsivity (R), response speed and detectivity (D^*). In Table 2 [13, 14, 16, 27, 29], their definitions and computing methods are summarized.

3.1 Phototransistors

When a photoconductor is exposed to light, the photo excited electron and hole can increase its conductivity. Under an external bias, the photo exited electron and hole will draft to opposite contact electrodes, and result in the generation of photocurrent. If one type of photo generated carries is trapped and another one could circulate many times through an external circuit before recombination with trapped ones, the device can produce a photo gain.

To improve the photosensitivity of photodetectors, two strategies are general used: one is maximizing their electrical response to light by improving the photo gain effect, another one is to minimize the noise of electrical output. The carrier density in the semiconductor can be modulated effectively by applying a gate voltage V_G, so that the device can be worked in the depletion regime by switching off the dark current. Therefore, the photo gain effect and low noise current can be achieved in phototransistors simultaneously, resulting in a high photosensitivity.

For b-P based phototransistors, a large responsivity of 9×10^4 A/W in the ultraviolet region has been reported (Figure 5(a-i)) [62]. With increasing incident light wavelength, the photoresponse of the photo-

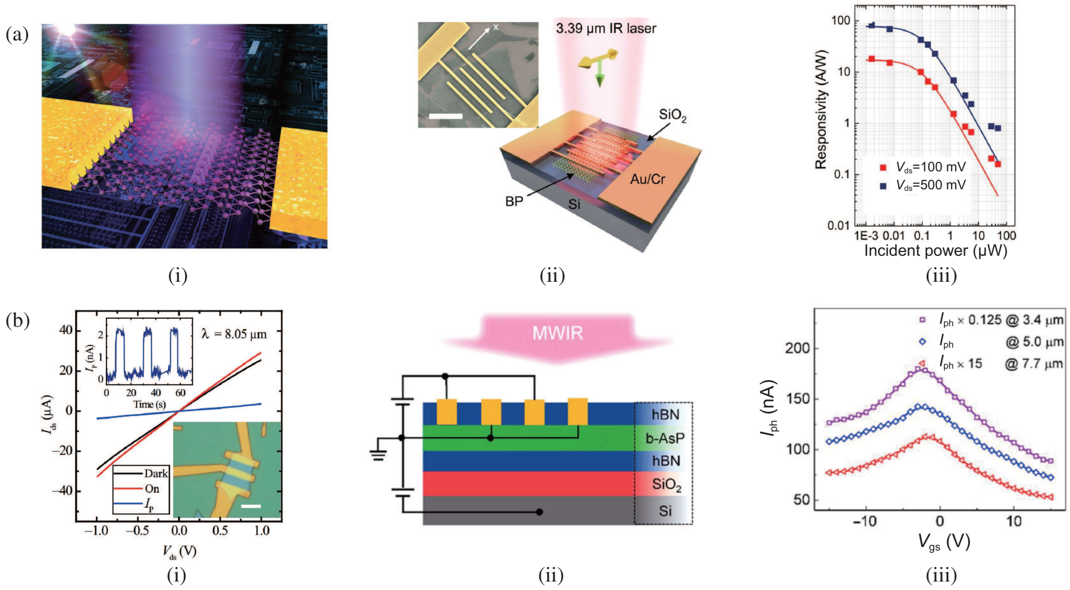

Figure 5 (Color online) Phototransistors based on b-P and b-AsP. (a-i) Device structure of few-layer b-P based phototransistor operating at UV light. (a-ii) Device structure of the b-P based photodetector for infrared detection. Inset: optical image of the phototransistor. (a-iii) The responsivity as a function of incident light power at $V_{ds} = 100$ mV and $V_{ds} = 500$ mV, respectively. (b-i) Photo response of a b-AsP based phototransistor operating at 8.05 μm with a power density of 0.17 $W \cdot cm^{-2}$. Inset: optical image of this device. (b-ii) Cross-sectional diagram of the phototransistor based on hBN/b-$As_{0.83}P_{0.17}$/hBN heterostructure. (b-iii) The photocurrent as a function of V_{gs}. (a-i) is reproduced with permission from [62], (a-ii) and (a-iii) from [57], (b-i) from [13], and (b-ii) and (b-iii) from [29].

transistor decreases rapidly, but the response rate is improved. Buscema et al. [61] reported a b-P based phototransistor with ultrafast photoresponse. A rise time of 1 ms and fall time of 4 ms were achieved at a wavelength of 940 nm, while the responsivity of the phototransistor is only 4.8 mA/W. The tradeoff between responsivity and response speed is very common in phototransistors, and this relationship is usually attributed to the photogating mechanism in 2D phototransistors. Guo et al. [57] first fabricated a b-P based mid-infrared phototransistor with a 10 nm-thick nanosheet (Figure 5(a-ii)). The device can detect an infrared light at a wavelength of 3.39 μm. At the same time, this device exhibits high photo gain with a responsivity of 82 A/W (Figure 5(a-iii)) [57]. Besides the high photosensitivity, the device can be effectively modulated at a frequency of kilohertz, owing to the fast carrier dynamics of b-P. The detection range of mid infrared spectrum is technological interest and scientific importance, which involves many important applications, including optical radar, free space communication, remote sensing and molecular fingerprint imaging.

Compared with phototransistors based on b-P, a distinguishing feature of b-AsP based phototransistors is their photoresponse at longer wavelengths. The optical image of a typical b-AsP based phototransistor is shown in Figure 5(b-i) (bottom inset). A significant photo response under a mid-infrared light at the wavelength of 8.05 μm is shown in Figure 5(b-i) (upper inset). Furthermore, the phototransistor shows a high response speed with a rise time of 0.54 ms and a delay time of 0.52 ms. As the increasing of bias voltage, the photocurrent ($I_P = I_{light} - I_{dark}$) increases linearly at $V_{gs} = 0$ V (Figure 5(b-i)) [13]. Yuan et al. [29] have fabricated a b-$As_{0.83}P_{0.17}$ photodetector sandwiched between layers of hBN (Figure 5(b-ii)). With the increasing of wavelength of incident light from 3.4 to 7.7 μm, the peak responsivity of phototransistor decreases from 190 to 1.2 mA/W at room temperature (Figure 5(b-iii)). Owing to the protection with hBN, the b-$As_{0.83}P_{0.17}$ photodetector reaches excellent air stability. In addition, the photo response of b-AsP can be maximized by adjusting the thickness of the material, and the dark current can also be minimized leading to a large detectivity. Amani et al. [27] reported a peak detectivity of 2.4×10^{10} $cm \cdot Hz^{1/2} \cdot W^{-1}$ for phototransistors of 36 nm-thick b-AsP (91% As) at room temperature. Compared with commercial mid-infrared detectors, the peak detectivity of the b-AsP (91% As) based phototransistor is improved by one order of magnitude [27]. In summary, the broad photoresponse in the mid-infrared region arising from the intrinsic bandgap, together with the improvement of stability in air condition, makes b-AsP a promising material for photodetector application in the mid-infrared range.

3.2 Photodiodes

In photodiodes, space charge region is formed at the p-n junction or Schottky junction between metal and semiconductors, resulting in build-in field. Under the light, photo generated carriers are driven by the built-in potential, moving to opposite electrodes.

Figure 6(a-i) shows an electrically tunable diode based on a vdW p-n heterojunction, fabricating by a p-type b-P and a n-type monolayer MoS_2 flake. The back gate voltage can modulate the current-rectifying characteristics of the device [96]. With the decreasing of back gate voltage, the rectification ratio (the ratio of the forward to reverse current) increases obviously. In the device, a peak rectification ratio of 10^5 can be obtained at $V_{\rm gs} = -30$ V through applying a bias voltage from -2 V to 2 V. Under a 633 nm laser with different incident power, the current of the photodiode increases obviously as shown in Figure 6(a-ii). A peak responsivity of 418 mA/W and external quantum efficiency of 0.3% at a bias of -2 V, can be abstracted from the I-V curves of the p-n diode [96]. Furthermore, a few-layer MoS_2/b-P heterojunction based photodiode is fabricated to detect near-infrared at room temperature, achieving a peak detectivity of 2.13×10^9 cm·Hz$^{1/2}$·W^{-1} at $\lambda = 1550$ nm [99]. By using a b-P vertical p-n junction, Yuan et al. [97] designed a polarization-sensitive broadband photodetector. In order to collect the photo generated hot carrier in an isotropic manner, the metal electrodes acting as the photocurrent collector are designed as ring shape; therefore the possibility of the photocurrent arising from geometric edge effect at the metal-b-P edge can be excluded [97]. Within the ring shape electrode, the photocurrent excited by 90° polarization light is far less than that by 0° light polarization, indicating that the intrinsic polarization dependent photo response arises from the b-P itself [97]. Photodetectors based on in-plane b-P p-n homojunctions have also been reported, which are defined by local electrostatic gating or chemical doping methods and exhibit an enhanced photo response [63, 105]. In addition, high-quality InSe/b-P vertical PN heterojunction has been reported. The heterojunction has an atomic-level flat interface and a perfect crystal lattice. The ballistic avalanche phenomenon is observed, and five orders of magnitude current jumps occur in this device. This device can be used as mid infrared photodetector, showing very high photon amplification (more than 10000) and lower noise performance than the theoretical limit of traditional avalanche photodetectors [57].

As for b-AsP-based vdW photodetectors, an attractive research direction is to build mid-infrared photodiodes. Long et al. [13] fabricated photodiodes using p-type b-AsP and n-type MoS_2. A vdW p-n junction can be formed using b-AsP and MoS_2, and the current under forward bias is higher than that under reverse bias more than two orders of magnitude. In the 3 to 5 μm range, the detectivity of this device is consistently larger than 4.9×10^9 cm·Hz$^{1/2}$·W^{-1} with a peak value about 9.2×10^9 cm·Hz$^{1/2}$·W^{-1} (Figure 6(b-i)) [13].

With the proper band alignment design of b-AsP-based heterojunctions, high-performance photodiodes can be realized. Wu et al. [14] designed a vertically stacked vdW heterojunction tunneling device of b-AsP and indium selenide (Figure 6(b-ii), inset), showing an unusual ultralow forward current below picoampere. Moreover, a record high reverse rectification ratio more than 10^7 is achieved in this device (Figure 6(b-ii)). The vdW heterojunction tunneling device functions as a sensitive photodiode in the visible wavelength range, as a result, an ultrahigh light on/off ratio about 1×10^7 is achieved. At the same time, the device exhibits a high detectivity of over 1×10^{12} cm·Hz$^{1/2}$·W^{-1} and a comparable responsivity of about 1 A/W [14]. Wu et al. [16] also designed a sensitive photodiode based on b-AsP/MoS_2 vdW heterojunction, in which the narrow gap b-AsP was utilized as an effective carrier selective contact with a unilateral depletion region band design. From the atomic force microscope image of this device, the thicknesses of b-AsP and MoS_2 are measured to be 59 and 66 nm, respectively. The heterojunction shows high sensitive at visible wavelength, but is not sensitive at infrared wavelength, because the photo response of this device mainly comes from MoS_2 flake [16]. To reveal the mechanism of this device, energy band diagram of b-AsP/MoS_2 heterojunction is drawn. When the device is illuminated under a 520-nm light, the photo carriers in the device mainly are generated in the thick MoS_2 channel. Because a large unilateral depletion region is formed in the MoS_2 side, the photo generated electrons in MoS_2 can draft to the b-AsP side freely and be collected by the drain electrode, while the photo generated holes will draft from the MoS_2 side to the source electrode [16]. This device achieves a record high response speed for photovoltaic detectors based on 2D vdW heterostructures, with a rise time of 9 μs and a fall time of 5 μs. This ultrafast response speed results from that the interface trapping effect is reduced significantly in the unilateral depletion region, and the photo generated electrons could recombine with the holes in the accumulation region rapidly [16].

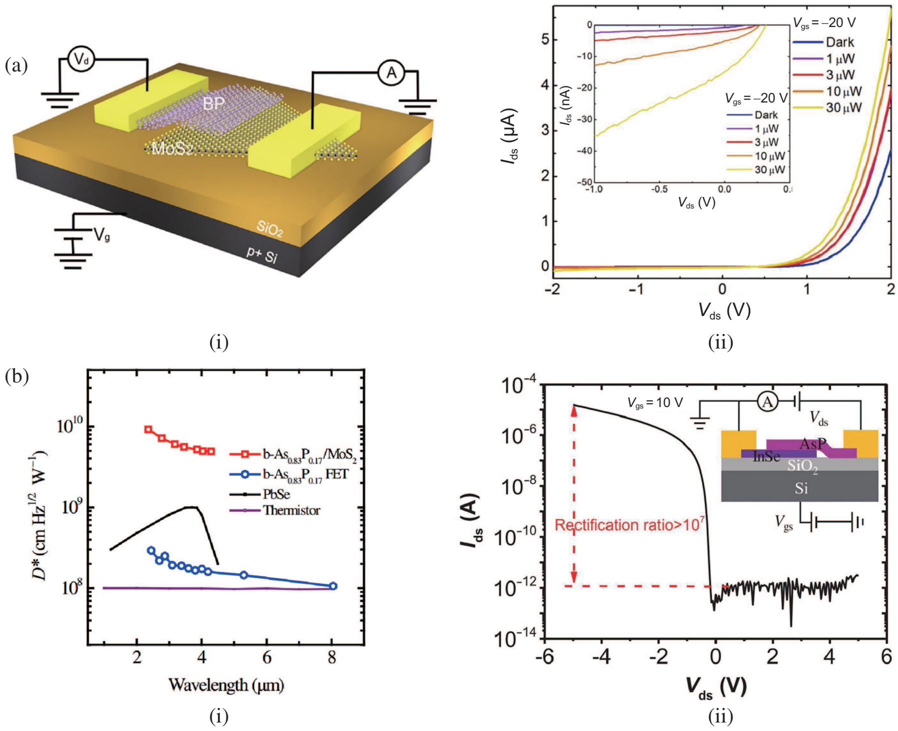

Figure 6 (Color online) Photodiodes based on b-P and b-AsP. (a-i) Schematic of the monolayer MoS_2/b-AsP photodiode. (a-ii) I_{ds}-V_{ds} curves of the p-n photodiode based on monolayer MoS_2/b-AsP under the incident light with various powers. Inset: the detailed reverse region at bias from −1 V to 0 V. (b-i) The detectivity as a function of wavelength at V_{ds} = 0 V. Compared with the detectivity of commercial thermistor bolometer [106] and PbSe mid-infrared detectors, the MoS_2/b-AsP photodiode shows great advantages. (b-ii) I_{ds}-V_{ds} curve of the InSe/b-AsP diode at V_{gs} = 10 V. Inset: schematic of the device. (a-i) and (a-ii) are reproduced with permission from [96], (b-i) from [13], and (b-iii) from [14].

4 Perspectives

First, the highest reported mobility of b-P is about 5200 $cm^2 \cdot V^{-1} \cdot s^{-1}$, which approaches its theoretical value. However, the highest mobility reported for b-AsP to date is only 307 $cm^2 \cdot V^{-1} \cdot s^{-1}$, which is much lower than the theoretically calculated value of 10000 $cm^2 \cdot V^{-1} \cdot s^{-1}$. As shown in Table 1, the mobility of b-P can be improved through proper contact electrodes, passivation layers and doping methods, which provides some directions for the improvement of the electronic properties of b-AsP. In addition, electronic anisotropy is another interesting property of b-AsP. The lattice periodicities are different along with different crystallographic directions, which results in anisotropy in crystal lattice. Generally, anisotropy in 2D materials is more pronounced owing to their atomic thickness. Electronic anisotropy is important for future multifunctional directional photodetectors based on b-AsP. Beyond that, according to the existing work in theory, there are still some properties and models to be verified for b-AsP, including the optical and transport bandgaps of monolayer material, the crystal structures with different components, and the key factors limiting the hole and electron mobility.

Second, as shown in Table 2, b-AsP based mid-infrared photodetectors show great advantages with respect to other 2D materials because of its small bandgap. However, detectivity and responsivity of b-AsP based mid-infrared photodetectors are lower than 1×10^{10} $cm \cdot Hz^{1/2} \cdot W^{-1}$ and 1 A/W, respectively, indicating a weak photo detection ability. To improve the photo detection ability of b-AsP, enhancing the photogating effect of the photodetectors presents a valuable research direction. Several methods such as designing waveguide or nanoplasmonics, p-type or n-type doping, or metal-doping, have been applied to enhance the photodetector performance of b-P (Table 3 [54, 56, 61–66, 84, 96–98, 101, 102, 104, 105, 107–109, 111]) and may also be applicable to b-AsP. To achieve high-performance infrared photodetectors, the thickness of b-AsP needs to be optimized, because it influences the optoelectronic properties of the photodetectors (Table 2). In addition, flexible mid-infrared photodetectors are one of the most important research directions in the field of wearable devices in the future, and they have great potential in the human health sector for pulse detection, blood oxygen detection, and body temperature detection.

Table 3 Performance of b-P based photodetectors[a)]

Material	Th (nm)	Device structure	Wavelength (nm)	R (mA/W)	EQE (%)	Speed (ms)	D^* (cm^2 V^{-1} s^{-1})	Ref.
b-P	8	Phototransistor	640	4.8	–	1, 4	–	[61]
b-P	4.5	Phototransistor	UV	9×10^7	–	1, 4	3×10^{13}	[62]
p-n b-P	10	Phototransistor	1550	5×10^3	390	0.035, 0.04	–	[105]
b-P	12	Phototransistor	3390	8.2×10^4	–	–	–	[107]
b-P-$\mathrm{C_{S2}CO_3}$	4.8	Phototransistor	405	1.88	576	–	–	[65]
b-P-$\mathrm{MoO_3}$				2.56	784			
Se doped b-P	–	Phototransistor	635	1.53×10^4	2993	–	–	[66]
b-P	–	Phototransistor	1550	6	–	0.1, 0.3	–	[84]
$\mathrm{WSe_2}$-BP-$\mathrm{MoS_2}$	–	Phototransistor	532	6.32×10^3	–	–	1.25×10^{11}	[102]
			1550	1.12×10^3	–	–	2.1×10^{10}	
b-P	10	Phototransistor	830	5.3×10^4	–	–	–	[54]
b-P	7	Phototransistor	830	18.7	–	–	–	[56]
b-P	<10	Photodiode	650	3.5	–	2	–	[104]
b-P-$\mathrm{MoS_2}$	22, 12	Photodiode	1550	153.4	20	0.015	3.1×10^{11}	[98]
			532	2.23×10^4	1000	–	2.13×10^9	
p-n b-P	–	Photodiode	940	–	0.1	–	–	[63]
b-P-$\mathrm{MoS_2}$	11, 0.9	Photodiode	633	418	0.3	–	–	[96]
p-n b-P	30	Photodiode	1200	0.35	–	–	–	[97]
b-P-InSe	–	Photodiode	455	11.7	3.2	24, 32	–	[108]
b-P	135	Plasmonics	1550	12	–	–	–	[101]
b-P	20	Plasmonics	1550	1×10^4	–	–	–	[64]
b-P	40	Waveguide	3825	1.13×10^4	–	–	–	[109]
b-P	36.8	Waveguide	2000	306.7	–	–	–	[111]
b-P	23	Waveguide	3700	2×10^3	–	–	–	[107]
	40		3700	2.3×10^4				
b-P	11	Waveguide	1570–1580	135	–	–	–	[104]
	100			675		3×10^{-7}		

a) p-n: p-n junction. Th: thickness. R: responsivity. EQE: external quantum efficiency. D^*: detectivity.

Flexible photodetectors based on b-AsP have not been studied to date and require further investigation.

Third, the distinctive band structure of b-AsP provides many opportunities for further band structure engineering. In combination with other 2D materials, the 2D heterostructure devices can be designed. 2D heterojunctions, such as b-AsP/$\mathrm{MoS_2}$ or b-AsP/InSe, have been fabricated with excellent rectification effect and photodetector performance. Besides 2D structures, 3D/b-AsP, 1D/b-AsP, and even 0D/b-AsP heterostructures are future research focuses for the development of novel devices beyond photodetectors.

Finally, in addition to fabricating novel devices and improving the performance of existing devices, there are still challenges to realize their practical applications. One of the major challenges is that the few-layer b-P and b-AsP are unstable in atmosphere. The performance of devices will be degraded because of the undesired reaction of b-P (or b-AsP) with water and oxygen. Passivation of the surface of b-P and b-AsP by depositing $\mathrm{Al_2O_3}$ thin films or encapsulating hBN layer has been proven to be the effective way to protect the material. Another strategy to keep the quality of materials and device performance is to decorate the surface with organic molecules. But, these methods still cannot prevent the degradation of b-P and b-AsP absolutely over a long period of time. It is still necessary to explore more effective and convenient passivation strategies. Another one challenge is to grow large area 2D b-P and b-AsP. Mechanical exfoliation method has been widely used to fabricate 2D b-P and b-AsP samples, however, the samples just can be used to demonstrate proof-of-concept device because of their small size. To realize practical electronic or optoelectronic systems, it is essential to grow large area b-P and b-AsP, which still is a huge challenge. Chemical vapor deposition (CVD) method has been demonstrated to grow high quality 2D materials with large area. Maybe it is a promising direction to fabricate large area 2D b-P and b-AsP in the future.

5 Summary

In this review, we summarized the properties of 2D b-P and b-AsP and the recent progress on their applications as photodetectors. The distinguished properties of 2D b-AsP, including high carrier mobility and proper bandgap make it a good tradeoff between transition metal dichalcogenides and graphene, as well as a promising material for high performance electronic and optoelectronic devices. Although some achievements have been made, many challenges and opportunities remain to further improve the photodetector performance.

References

1 Bridgman P W. Two new modifications of phosphorus. J Am Chem Soc, 1914, 36: 1344–1363

2 Morita A. Semiconducting black phosphorus. Appl Phys A, 1986, 39: 227–242

3 Wang X R, Zhou P. Special focus on two-dimensional materials and device applications. Sci China Inf Sci, 2019, 62: 220400

4 Yang H, Xiao M Q, Cui Y, et al. Nonvolatile memristor based on heterostructure of 2D room-temperature ferroelectric α-In_2Se_3 and WSe_2. Sci China Inf Sci, 2019, 62: 220404

5 Jia R D, Chen L, Huang Q Q, et al. Complementary tunneling transistors based on WSe_2/SnS_2 van der Waals heterostructure. Sci China Inf Sci, 2020, 63: 149401

6 Liu L T, Liu Y, Duan X F. Graphene-based vertical thin film transistors. Sci China Inf Sci, 2020, 63: 201401

7 Novoselov K S, Geim A K, Morozov S V, et al. Electric field effect in atomically thin carbon films. Science, 2004, 306: 666–669

8 Tran V, Soklaski R, Liang Y, et al. Layer-controlled band gap and anisotropic excitons in few-layer black phosphorus. Phys Rev B, 2014, 89: 235319

9 Liu H, Neal A T, Zhu Z, et al. Phosphorene: an unexplored 2D semiconductor with a high hole mobility. ACS Nano, 2014, 8: 4033–4041

10 Li L, Yu Y, Ye G J, et al. Black phosphorus field-effect transistors. Nat Nanotech, 2014, 9: 372–377

11 Shirotani I, Mikami J, Adachi T, et al. Phase transitions and superconductivity of black phosphorus and phosphorus-arsenic alloys at low temperatures and high pressures. Phys Rev B, 1994, 50: 16274–16278

12 Liu B, Köpf M, Abbas A N, et al. Black arsenic-phosphorus: layered anisotropic infrared semiconductors with highly tunable compositions and properties. Adv Mater, 2015, 27: 4423–4429

13 Long M, Gao A, Wang P, et al. Room temperature high-detectivity mid-infrared photodetectors based on black arsenic phosphorus. Sci Adv, 2017, 3: e1700589

14 Wu F, Xia H, Sun H, et al. AsP/InSe van der Waals tunneling heterojunctions with ultrahigh reverse rectification ratio and high photosensitivity. Adv Funct Mater, 2019, 29: 1900314

15 Ryzhii V, Ryzhii M, Mitin V, et al. Far-infrared photodetectors based on graphene/black-AsP heterostructures. Opt Express, 2020, 28: 2480–2498

16 Wu F, Li Q, Wang P, et al. High efficiency and fast van der Waals hetero-photodiodes with a unilateral depletion region. Nat Commun, 2019, 10: 4663

17 Takao Y, Asahina H, Morita A. Electronic structure of black phosphorus in tight binding approach. J Phys Soc Jpn, 1981, 50: 3362–3369

18 Asahina H, Shindo K, Morita A. Electronic structure of black phosphorus in self-consistent pseudopotential approach. J Phys Soc Jpn, 1982, 51: 1193–1199

19 Xia F, Wang H, Jia Y. Rediscovering black phosphorus as an anisotropic layered material for optoelectronics and electronics. Nat Commun, 2014, 5: 4458

20 Xia F, Wang H, Hwang J C M, et al. Black phosphorus and its isoelectronic materials. Nat Rev Phys, 2019, 1: 306–317

21 Zhou W, Zhang S, Wang Y, et al. Anisotropic in-plane ballistic transport in monolayer black arsenic-phosphorus FETs. Adv Electron Mater, 2020, 6: 1901281

22 Shi X, Wang T, Wang J, et al. Synthesis of black arsenic-phosphorus and its application for Er-doped fiber ultrashort laser generation. Opt Mater Express, 2019, 9: 2348–2357

23 Sun J, Lin N, Ren H, et al. The electronic structure, mechanical flexibility and carrier mobility of black arsenic-phosphorus monolayers: a first principles study. Phys Chem Chem Phys, 2016, 18: 9779–9787

24 Sun Y, Shuai Z, Wang D. Lattice thermal conductivity of monolayer AsP from first-principles molecular dynamics. Phys Chem Chem Phys, 2018, 20: 14024–14030

25 Karki B, Rajapakse M, Sumanasekera G U, et al. Structural and thermoelectric properties of black arsenic-phosphorus. ACS Appl Energy Mater, 2020, 3: 8543–8551

26 Li L L, Bacaksiz C, Nakhaee M, et al. Single-layer Janus black arsenic-phosphorus (b-AsP): optical dichroism, anisotropic vibrational, thermal, and elastic properties. Phys Rev B, 2020, 101: 134102

27 Amani M, Regan E, Bullock J, et al. Mid-wave infrared photoconductors based on black phosphorus-arsenic alloys. ACS Nano, 2017, 11: 11724–11731

28 Yu L, Zhu Z, Gao A, et al. Electrically tunable optical properties of few-layer black arsenic phosphorus. Nanotechnology, 2018, 29: 484001

29 Yuan S, Shen C, Deng B, et al. Air-stable room-temperature mid-infrared photodetectors based on hBN/black arsenic phosphorus/hBN heterostructures. Nano Lett, 2018, 18: 3172–3179

30 Low T, Rodin A S, Carvalho A, et al. Tunable optical properties of multilayer black phosphorus thin films. Phys Rev B, 2014, 90: 075434

31 Young E P, Park J, Bai T, et al. Wafer-scale black arsenic-phosphorus thin-film synthesis validated with density functional perturbation theory predictions. ACS Appl Nano Mater, 2018, 1: 4737–4745

32 Li L, Kim J, Jin C, et al. Direct observation of the layer-dependent electronic structure in phosphorene. Nat Nanotech, 2017, 12: 21–25

33 Fei R, Yang L. Strain-engineering the anisotropic electrical conductance of few-layer black phosphorus. Nano Lett, 2014, 14: 2884–2889

34 Benam Z H, Arkin H, Aktürk E. Point defects in buckled and asymmetric washboard phases of arsenic phosphorus: a first principles study. Comput Mater Sci, 2017, 140: 290–298

35 Li Y, Hu Z, Lin S, et al. Giant anisotropic raman response of encapsulated ultrathin black phosphorus by uniaxial strain. Adv Funct Mater, 2017, 27: 1600986

36 Wang X, Jones A M, Seyler K L, et al. Highly anisotropic and robust excitons in monolayer black phosphorus. Nat Nanotech, 2015, 10: 517–521

37 Kim J, Lee J U, Lee J, et al. Anomalous polarization dependence of Raman scattering and crystallographic orientation of black phosphorus. Nanoscale, 2015, 7: 18708–18715

38 Wu J, Mao N, Xie L, et al. Identifying the crystalline orientation of black phosphorus using angle-resolved polarized raman spectroscopy. Angew Chem Int Ed, 2015, 54: 2366–2369

39 Phaneuf-L'Heureux A L, Favron A, Germain J F, et al. Polarization-resolved raman study of bulk-like and davydov-induced vibrational modes of exfoliated black phosphorus. Nano Lett, 2016, 16: 7761–7767

40 Viti L, Hu J, Coquillat D, et al. Efficient terahertz detection in black-phosphorus nano-transistors with selective and controllable plasma-wave, bolometric and thermoelectric response. Sci Rep, 2016, 6: 20474

41 Liu Y, Qiu Z, Carvalho A, et al. Gate-tunable giant stark effect in few-layer black phosphorus. Nano Lett, 2017, 17: 1970–1977

42 Das S, Demarteau M, Roelofs A. Ambipolar phosphorene field effect transistor. ACS Nano, 2014, 8: 11730–11738

43 Engel M, Steiner M, Avouris P. Black phosphorus photodetector for multispectral, high-resolution imaging. Nano Lett, 2014, 14: 6414–6417

44 Hong T, Chamlagain B, Lin W, et al. Polarized photocurrent response in black phosphorus field-effect transistors. Nanoscale, 2014, 6: 8978–8983

45 Avsar A, Vera-Marun I J, Tan J Y, et al. Air-stable transport in graphene-contacted, fully encapsulated ultrathin black phosphorus-based field-effect transistors. ACS Nano, 2015, 9: 4138–4145

46 Li L, Ye G J, Tran V, et al. Quantum oscillations in a two-dimensional electron gas in black phosphorus thin films. Nat Nanotech, 2015, 10: 608–613

47 Saito Y, Iwasa Y. Ambipolar insulator-to-metal transition in black phosphorus by ionic-liquid gating. ACS Nano, 2015, 9: 3192–3198

48 Viti L, Hu J, Coquillat D, et al. Black phosphorus terahertz photodetectors. Adv Mater, 2015, 27: 5567–5572

49 Yang J, Xu R, Pei J, et al. Optical tuning of exciton and trion emissions in monolayer phosphorene. Light Sci Appl, 2015, 4: e312

50 Zhu W, Yogeesh M N, Yang S, et al. Flexible black phosphorus ambipolar transistors, circuits and AM demodulator. Nano Lett, 2015, 15: 1883–1890

51 Li L, Yang F, Ye G J, et al. Quantum hall effect in black phosphorus two-dimensional electron system. Nat Nanotech, 2016, 11: 593–597

52 Zhu W, Park S, Yogeesh M N, et al. Black phosphorus flexible thin film transistors at gighertz frequencies. Nano Lett, 2016, 16: 2301–2306

53 Dhanabalan S C, Ponraj J S, Guo Z, et al. Emerging trends in phosphorene fabrication towards next generation devices. Adv Sci, 2017, 4: 1600305

54 Miao J, Song B, Li Q, et al. Photothermal effect induced negative photoconductivity and high responsivity in flexible black phosphorus transistors. ACS Nano, 2017, 11: 6048–6056

55 Miao J, Xu Z, Li Q, et al. Vertically stacked and self-encapsulated van der Waals heterojunction diodes using two-dimensional layered semiconductors. ACS Nano, 2017, 11: 10472–10479

56 Miao J, Song B, Xu Z, et al. Single pixel black phosphorus photodetector for near-infrared imaging. Small, 2018, 14: 1702082

57 Gao A, Lai J, Wang Y, et al. Observation of ballistic avalanche phenomena in nanoscale vertical InSe/BP heterostructures. Nat Nanotechnol, 2019, 14: 217–222

58 Qiao J, Kong X, Hu Z X, et al. High-mobility transport anisotropy and linear dichroism in few-layer black phosphorus. Nat Commun, 2014, 5: 4475

59 Xie M, Zhang S, Cai B, et al. A promising two-dimensional solar cell donor: black arsenic-phosphorus monolayer with 1.54 eV direct bandgap and mobility exceeding 14000 $\mathrm{cm^2V^{-1}s^{-1}}$. Nano Energy, 2016, 28: 433–439

60 Kim J S, Liu Y, Zhu W, et al. Toward air-stable multilayer phosphorene thin-films and transistors. Sci Rep, 2015, 5: 8989

61 Buscema M, Groenendijk D J, Blanter S I, et al. Fast and broadband photoresponse of few-layer black phosphorus field-effect transistors. Nano Lett, 2014, 14: 3347–3352

62 Wu J, Koon G K W, Xiang D, et al. Colossal ultraviolet photoresponsivity of few-layer black phosphorus. ACS Nano, 2015, 9: 8070–8077

63 Buscema M, Groenendijk D J, Steele G A, et al. Photovoltaic effect in few-layer black phosphorus PN junctions defined by local electrostatic gating. Nat Commun, 2014, 5: 4651

64 Chen C, Youngblood N, Peng R, et al. Three-dimensional integration of black phosphorus photodetector with silicon photonics and nanoplasmonics. Nano Lett, 2017, 17: 985–991

65 Xiang D, Han C, Wu J, et al. Surface transfer doping induced effective modulation on ambipolar characteristics of few-layer black phosphorus. Nat Commun, 2015, 6: 6485

66 Xu Y, Yuan J, Fei L, et al. Selenium-doped black phosphorus for high-responsivity 2D photodetectors. Small, 2016, 12: 5000–5007

67 Na J, Park K, Kim J T, et al. Air-stable few-layer black phosphorus phototransistor for near-infrared detection. Nanotechnology, 2017, 28: 085201

68 Chen X, Wu Y, Wu Z, et al. High-quality sandwiched black phosphorus heterostructure and its quantum oscillations. Nat Commun, 2015, 6: 7315

69 Tayari V, Hemsworth N, Fakih I, et al. Two-dimensional magnetotransport in a black phosphorus naked quantum well. Nat Commun, 2015, 6: 7702

70 Long G, Maryenko D, Shen J, et al. Achieving ultrahigh carrier mobility in two-dimensional hole gas of black phosphorus. Nano Lett, 2016, 16: 7768–7773

71 Perello D J, Chae S H, Song S, et al. High-performance n-type black phosphorus transistors with type control via thickness and contact-metal engineering. Nat Commun, 2015, 6: 7809

72 Prakash A, Cai Y, Zhang G, et al. Black phosphorus n-type field-effect transistor with ultrahigh electron mobility via aluminum adatoms doping. Small, 2017, 13: 1602909

73 Koenig S P, Doganov R A, Seixas L, et al. Electron doping of ultrathin black phosphorus with Cu adatoms. Nano Lett, 2016, 16: 2145–2151

74 Du Y, Liu H, Deng Y, et al. Device perspective for black phosphorus field-effect transistors: contact resistance, ambipolar

behavior, and scaling. ACS Nano, 2014, 8: 10035–10042
75 Wang Y, Wu P, Wang Z, et al. Air-stable low-symmetry narrow-bandgap 2D sulfide niobium for polarization photodetection. Adv Mater, 2020, 32: 2005037
76 Hu W-D, Li Q, Chen X-S, et al. Recent progress on advanced infrared photodetectors. Acta Phys Sin, 2019, 68: 120701
77 Wang Z, Wang P, Wang F, et al. A noble metal dichalcogenide for high-performance field-effect transistors and broadband photodetectors. Adv Funct Mater, 2020, 30: 1907945
78 Ziletti A, Carvalho A, Trevisanutto P E, et al. Phosphorene oxides: bandgap engineering of phosphorene by oxidation. Phys Rev B, 2015, 91: 085407
79 Ziletti A, Carvalho A, Campbell D K, et al. Oxygen defects in phosphorene. Phys Rev Lett, 2015, 114: 046801
80 Utt K L, Rivero P, Mehboudi M, et al. Intrinsic defects, fluctuations of the local shape, and the photo-oxidation of black phosphorus. ACS Cent Sci, 2015, 1: 320–327
81 Yang T, Dong B, Wang J, et al. Interpreting core-level spectra of oxidizing phosphorene: theory and experiment. Phys Rev B, 2015, 92: 125412
82 Favron A, Gaufrés E, Fossard F, et al. Photooxidation and quantum confinement effects in exfoliated black phosphorus. Nat Mater, 2015, 14: 826–832
83 Wood J D, Wells S A, Jariwala D, et al. Effective passivation of exfoliated black phosphorus transistors against ambient degradation. Nano Lett, 2014, 14: 6964–6970
84 Peng R, Khaliji K, Youngblood N, et al. Midinfrared electro-optic modulation in few-layer black phosphorus. Nano Lett, 2017, 17: 6315–6320
85 Cao Y, Mishchenko A, Yu G L, et al. Quality heterostructures from two-dimensional crystals unstable in air by their assembly in inert atmosphere. Nano Lett, 2015, 15: 4914–4921
86 Viti L, Hu J, Coquillat D, et al. Heterostructured hBN-BP-hBN nanodetectors at terahertz frequencies. Adv Mater, 2016, 28: 7390–7396
87 Illarionov Y Y, Waltl M, Rzepa G, et al. Long-term stability and reliability of black phosphorus field-effect transistors. ACS Nano, 2016, 10: 9543–9549
88 Artel V, Guo Q, Cohen H, et al. Protective molecular passivation of black phosphorus. npj 2D Mater Appl, 2017, 1: 6
89 Cai Y, Ke Q, Zhang G, et al. Highly itinerant atomic vacancies in phosphorene. J Am Chem Soc, 2016, 138: 10199–10206
90 Hu W, Yang J. Defects in phosphorene. J Phys Chem C, 2015, 119: 20474–20480
91 Liu C H, Chang Y C, Norris T B, et al. Graphene photodetectors with ultra-broadband and high responsivity at room temperature. Nat Nanotech, 2014, 9: 273–278
92 Roy K, Padmanabhan M, Goswami S, et al. Graphene-MoS_2 hybrid structures for multifunctional photoresponsive memory devices. Nat Nanotech, 2013, 8: 826–830
93 Lopez-Sanchez O, Lembke D, Kayci M, et al. Ultrasensitive photodetectors based on monolayer MoS_2. Nat Nanotech, 2013, 8: 497–501
94 Huo N, Konstantatos G. Ultrasensitive all-2D MoS_2 phototransistors enabled by an out-of-plane MoS_2 PN homojunction. Nat Commun, 2017, 8: 572
95 Tu L, Cao R, Wang X, et al. Ultrasensitive negative capacitance phototransistors. Nat Commun, 2020, 11: 101
96 Deng Y, Luo Z, Conrad N J, et al. Black phosphorus-monolayer MoS_2 van der Waals heterojunction p-n diode. ACS Nano, 2014, 8: 8292–8299
97 Yuan H, Liu X, Afshinmanesh F, et al. Polarization-sensitive broadband photodetector using a black phosphorus vertical p-n junction. Nat Nanotech, 2015, 10: 707–713
98 Guo Q, Pospischil A, Bhuiyan M, et al. Black phosphorus mid-infrared photodetectors with high gain. Nano Lett, 2016, 16: 4648–4655
99 Ye L, Li H, Chen Z, et al. Near-infrared photodetector based on MoS_2/black phosphorus heterojunction. ACS Photonics, 2016, 3: 692–699
100 Miao J, Zhang L, Wang C. Black phosphorus electronic and optoelectronic devices. 2D Mater, 2019, 6: 032003
101 Venuthurumilli P K, Ye P D, Xu X. Plasmonic resonance enhanced polarization-sensitive photodetection by black phosphorus in near infrared. ACS Nano, 2018, 12: 4861–4867
102 Li H, Ye L, Xu J. High-performance broadband floating-base bipolar phototransistor based on WSe_2/BP/MoS_2 heterostructure. ACS Photonics, 2017, 4: 823–829
103 Miao J, Zhang S, Cai L, et al. Black phosphorus schottky diodes: channel length scaling and application as photodetectors. Adv Electron Mater, 2016, 2: 1500346
104 Youngblood N, Chen C, Koester S J, et al. Waveguide-integrated black phosphorus photodetector with high responsivity and low dark current. Nat Photon, 2015, 9: 247–252
105 Xu Y, Liu C, Guo C, et al. High performance near infrared photodetector based on in-plane black phosphorus p-n homojunction. Nano Energy, 2020, 70: 104518
106 Hsu A L, Herring P K, Gabor N M, et al. Graphene-based thermopile for thermal imaging applications. Nano Lett, 2015, 15: 7211–7216
107 Huang L, Ang K W. Black phosphorus photonics toward on-chip applications. Appl Phys Rev, 2020, 7: 031302
108 Zhao S, Wu J, Jin K, et al. Highly polarized and fast photoresponse of black phosphorus-InSe vertical p-n heterojunctions. Adv Funct Mater, 2018, 28: 1802011
109 Ma Y, Dong B, Wei J, et al. High-responsivity mid-infrared black phosphorus slow light waveguide photodetector. Adv Opt Mater, 2020, 8: 2000337
110 Huang L, Dong B, Guo X, et al. Waveguide-integrated black phosphorus photodetector for mid-infrared applications. ACS Nano, 2019, 13: 913–921
111 Yin Y, Cao R, Guo J, et al. High-speed and high-responsivity hybrid silicon/black-phosphorus waveguide photodetectors at 2 μm. Laser Photon Rev, 2019, 556: 1900032